The Meteoritical Society

Meteoritics & Planetary Science 46, Nr 10, 1510–1524 (2011)
doi: 10.1111/j.1945-5100.2011.01246.x

Numerical modeling of oblique hypervelocity impacts on strong ductile targets

Thomas M. DAVISON[1*], Gareth S. COLLINS[1], Dirk ELBESHAUSEN[2], Kai WÜNNEMANN[2], and Anton KEARSLEY[3]

[1]Impacts and Astromaterials Research Centre, Department of Earth Science and Engineering, Imperial College London, London SW7 2AZ, UK
[2]Museum für Naturkunde, Leibniz-Institut, Humboldt-University of Berlin, D-10115 Berlin, Germany
[3]IARC, Department of Mineralogy, Natural History Museum, London SW7 5BD, UK
[*]Corresponding author. E-mail: tdavison@uchicago.edu

(Received 04 May 2011; revision accepted 08 July 2011)

Abstract–The majority of meteorite impacts occur at oblique incidence angles. However, many of the effects of obliquity on impact crater size and morphology are poorly understood. Laboratory experiments and numerical models have shown that crater size decreases with impact angle, the along-range crater profile becomes asymmetric at low incidence angles, and below a certain threshold angle the crater planform becomes elliptical. Experimental results at approximately constant impact velocity suggest that the elliptical threshold angle depends on target material properties. Herein, we test the hypothesis that the threshold for oblique crater asymmetry depends on target material strength. Three-dimensional numerical modeling offers a unique opportunity to study the individual effects of both impact angle and target strength; however, a systematic study of these two parameters has not previously been performed. In this work, the three-dimensional shock physics code iSALE-3D is validated against laboratory experiments of impacts into a strong, ductile target material. Digital elevation models of craters formed in laboratory experiments were created from stereo pairs of scanning electron microscope images, allowing the size and morphology to be directly compared with the iSALE-3D craters. The simulated craters show excellent agreement with both the crater size and morphology of the laboratory experiments. iSALE-3D is also used to investigate the effect of target strength on oblique incidence impact cratering. We find that the elliptical threshold angle decreases with decreasing target strength, and hence with increasing cratering efficiency. Our simulations of impacts on ductile targets also support the prediction from Chapman and McKinnon (1986) that cratering efficiency depends on only the vertical component of the velocity vector.

INTRODUCTION

The formation of impact craters caused by the hypervelocity collision of astronomical bodies is a key solar system process. Based on previous work of Gilbert (1893), Shoemaker (1962) showed that the majority of all impacts occur at oblique incidence angles. The probability, P, of an impact occurring with an incidence angle i (measured from the target plane) in the range θ to $\theta + \mathrm{d}\theta$ is given by:

$$P(\theta < i < \theta + \mathrm{d}\theta) \propto 2 \cdot \sin(\theta)\cos(\theta)\mathrm{d}\theta = \sin(2 \cdot \theta)\mathrm{d}\theta \quad (1)$$

This probability is independent of the gravity of the target planet, which means that the most common impact angle is 45°, and approximately 90% of all impacts occur at angles $< 70°$ from the target plane. It is therefore vital that we understand what effect impact angle has upon cratering processes.

The effect of impact angle on crater size and morphology has been studied directly through laboratory experiments (e.g., Gault and Wedekind 1978; Christiansen et al. 1993; Burchell and Mackay 1998) and indirectly through observations of impact craters using remote sensing techniques (e.g., Schultz and Lutz-Garihan 1982; Bottke et al. 2000). Craters formed at oblique angles of incidence differ from those produced by vertical impacts in several ways: (1) the size of the crater is known to decrease with decreasing incidence

angle (e.g., Gault and Wedekind 1978; Christiansen et al. 1993; Hayhurst et al. 1995; Burchell and Mackay 1998); (2) the shape of the crater profile along the trajectory of the impactor becomes more asymmetrical with decreasing impact angle (e.g., Gault et al. 1965; Burchell and Mackay 1998); and (3) the planform of the crater is circular at high incidence angles, but becomes elliptical below a certain threshold angle (e.g., Gault and Wedekind 1978; Christiansen et al. 1993; Burchell and Mackay 1998; Bottke et al. 2000). However, a thorough quantification of these effects and the relevance of observations from small-scale experiments to large-scale craters are yet to be established.

Numerical modeling provides a powerful complement to observational studies of impact processes. However, until recently, the majority of numerical modeling studies have used shock physics codes (historically called "hydrocodes") that operate in two dimensions, precluding the study of oblique impact. This is because 2D models typically employ an axial symmetry, which limits the simulation geometry to normal-incidence angle impacts (i.e., the velocity vector is perpendicular to the target surface), but reduces the complexity and computational expense of the calculation. To simulate impacts formed at oblique incidence angles, it is necessary to use three-dimensional numerical models, which are computationally more complex and expensive.

Recently, thanks in part to advances in computational resources, several pioneering papers have simulated impact events in three dimensions. Pierazzo and Melosh (2000a, 2000b, 2000c) studied impact melt production and shock wave propagation in the early stages of oblique impacts. In addition, full three-dimensional models of impact events (e.g., Artemieva et al. 2002, 2004; Ivanov and Artemieva 2002; Shuvalov 2003; Artemieva and Ivanov 2004; Gisler et al. 2004; Shuvalov and Trubetskaya 2007, 2008) have provided important insight into the effect of obliquity in specific case studies. There are fewer examples in the literature of using hydrocodes to systematically study the effects of changing impact angle (e.g., Hayhurst et al. 1995). Recently, Marinova et al. (2011) investigated the effects of impact angle on planetary-scale impact processes. A study by Elbeshausen et al. (2009) used the three-dimensional hydrocode iSALE-3D (Amsden and Ruppel 1981; Elbeshausen and Wünnemann 2011) to systematically investigate the effect of impact angle on crater size in strengthless and frictional targets over a wide range of projectile sizes. In this article, we build on those simulations in two ways. First, iSALE-3D is validated by simulating oblique impact cratering on metal targets, and comparing the results with data from equivalent laboratory impact experiments (Burchell and Mackay 1998). Second, the influence of target strength on crater size and asymmetry is quantified for oblique impacts on ductile materials. By reducing the shear strength of the material from that of aluminum to shear strength more applicable to planetary surfaces, some of the effects of impact obliquity studied here can be applied to planetary-scale cratering processes (this is discussed further in the Applicability to Impacts on Planets and Other Cosmic Bodies section).

BACKGROUND—OBLIQUE INCIDENCE ANGLE CRATERS

The Influence of Impact Angle on Crater Size

Small-scale impact experiments have demonstrated that impact crater size (width, length, depth, and volume) depends on the angle of impact to the target plane and that this dependence is affected by impactor and target properties (such as density and strength). In a seminal paper, Gault and Wedekind (1978) used light-gas gun experiments to explore the effect of impact angle upon cratering processes. They found that as impact angle decreases (i.e., for more oblique impact angles), the size of the crater decreases. To quantify this, they calculated the displaced mass of the crater and normalized it by the displaced mass for a vertical incidence crater. In particulate targets, the variation in displaced mass was proportional to $\sin(\theta)$, whereas in rock targets, the variation was proportional to $\sin^2(\theta)$. Based on analysis of these laboratory data, Chapman and McKinnon (1986) proposed that crater volume (comparable to measurements of displaced mass) scales only with the vertical component of velocity, rather than the total magnitude of the velocity. Elbeshausen et al. (2009) showed that although this assumption seems to hold for a cohesionless target material with a coefficient of internal friction of 0.7 (a typical value for sand), it does not hold for impacts in strengthless targets or cohesionless targets with a coefficient of internal friction much less than 0.7. They found that the effect of impact angle on crater dimensions depends on target material; for different friction coefficients the depth, along-range, and across-range dimensions were affected in different ways by changes in impact angle. Christiansen et al. (1993) showed that, for high strength, ductile metal targets, the maximum crater diameter and depth decrease with increasing obliquity. The metal–metal impact experiments of Burchell and Mackay (1998) showed that the effect of impact angle is dependent on the contrast between impactor and target density. According to those experiments, crater depth decreases with impact angle, in proportion to $\sin^b(\theta)$, where b decreases with increasing projectile density (for a given target density) and increases with increasing impact velocity. For an impact

velocity of 5 km s^{-1}, and when the target and projectile densities are the same (i.e., $\rho_p = \rho_t$), $b \approx 1$.

The Influence of Impact Angle on Crater Shape

Another consequence of reducing the impact angle to the target plane is that the crater shape becomes more asymmetrical (Gault et al. 1965; Gault and Wedekind 1978). At impact angles close to perpendicular, the along-range profile and the planform of the crater are both symmetrical. The deepest point is midway between the crater walls and the planform is circular. This symmetry in crater shape persists as impact angle is reduced until a threshold angle, θ_e, is reached. For impact angles less than this threshold angle, the crater planform is elliptical (most commonly longer in the direction of impact), the crater wall on the uprange side is steeper than the wall on the downrange side of the crater, and the deepest point along the profile is offset toward the uprange wall (e.g., Burchell and Mackay 1998).

Laboratory experiments have established that the elliptical crater threshold angle depends on target properties and impact velocity (Gault and Wedekind 1978; Christiansen et al. 1993; Burchell and Mackay 1998; see Table 1). Defining the elliptical crater threshold angle θ_e as the angle below which crater ellipticity (length/width) is greater than 1.1, laboratory impact experiments in sand suggest $\theta_e \approx 5°$, whereas identical experiments in rock (granite) suggest $\theta_e \approx 30°$ (Gault and Wedekind 1978). The elliptical crater threshold angle in strong ductile metal targets is similar to that for rock. The results of laboratory experiments suggest that for impacts of aluminum projectiles into aluminum targets, $\theta_e \approx 25°$ for an impact velocity of 7 km s^{-1} (Christiansen et al. 1993), and $\theta_e = 35$–$40°$ for an impact velocity of 5 km s^{-1} (Burchell and Mackay 1998). For other combinations of metallic targets and projectiles with comparable densities, the elliptical crater threshold varies from 20 to 50° (Burchell and Mackay 1998). From this summary, it is clear that the effect of impact angle on crater size and shape is different for impacts in different materials. In particular, some target property (or properties) must strongly influence the effect of impact angle on the asymmetry of the cratering process. A likely candidate is target strength (Gault and Wedekind 1978; Bottke et al. 2000). One aim of this article therefore is to use the three-dimensional shock physics code, iSALE-3D (Amsden and Ruppel 1981; Elbeshausen and Wünnemann 2011), to quantify the coupled effect of target strength and impact angle on crater asymmetry in impacts on ductile materials. We focus on ductile target materials, as these have been the subject of many well-documented laboratory experiments that allow us to validate our numerical model. Once validated, numerical models offer the advantage that any model parameter can be altered independently of all others in the simulation. This is not always possible in laboratory studies (for example, changing target strength may also change other material properties, e.g., density). Using this numerical model, we quantify the individual effect of target strength on oblique impact cratering.

Table 1. Ellipticity threshold angle for targets of different strength.

Target material	Threshold angle, θ_e (°)	Velocity (km s^{-1})	Cratering efficiency, $D_\perp/L$
Sand	4.75[a]	6.4	~ 60
Mars/Venus/Moon	12[b]		~ 10[c]
Lead	20–30[d]	5.0–5.3	~ 7
Aluminum	25[e]	5.5–6.2	~ 4
Granite	30[a]	2.1–7.0	
Aluminum	35–40[d]	4.9–5.3	~ 3.3
Aluminum (Y_0 = 2 MPa)	10–15[f]	5.0	11.8
Aluminum (Y_0 = 20 MPa)	15–20[f]	5.0	6.4
Aluminum (Y_0 = 200 MPa)	30–35[f]	5.0	3.5

Comparison of previous work showing the ellipticity threshold angle increases for higher strength targets (in other words, for lower cratering efficiency), and the modeling results of this study. Cratering efficiency is defined as the diameter of the crater divided by the diameter of the projectile.
[a]Gault and Wedekind (1978).
[b]Bottke et al. (2000).
[c]Holsapple (1993).
[d]Burchell and Mackay (1998).
[e]Christiansen et al. (1993).
[f]This work.

NUMERICAL MODELING

Hydrocode modeling is a powerful tool to study terrestrial and planetary impact cratering events. Hydrocodes (e.g., see Anderson 1987; Benson 1992; Pierazzo and Collins 2004) solve a finite difference approximation of the equations of conservation of mass, momentum, and energy. They simulate the response of solids and fluids to deforming forces and the formation and propagation of shock waves within a finite grid of cells. Many hydrocodes operate in the two-dimensional domain. Thus, they have to rely on axial symmetry, which limits calculations to vertical impacts only. In this study, we use iSALE-3D, one advantage of which is that it allows for impacts of all angles and therefore allows the full parameter space of oblique impacts to be studied.

iSALE-3D is a multimaterial, finite difference shock physics code used for simulating impact processes. A detailed description of the development history of iSALE-3D is presented in Elbeshausen et al. (2009) and Elbeshausen and Wünnemann (2011). It follows a similar approach to the 2D code iSALE (Collins et al. 2004; Wünnemann et al. 2006). Both iSALE and iSALE-3D inherit much of their underlying structure from SALE/SALE3D (Amsden et al. 1980; Amsden and Ruppel 1981), and extensions of these two codes specifically developed for impact applications (Melosh et al. 1992; Ivanov et al. 1997; Ivanov and Artemieva 2002; Ivanov 2005). iSALE is well tested against laboratory experiments at low and high strain rates (Wünnemann et al. 2008) and both codes have been benchmarked against other hydrocodes (Pierazzo et al. 2008). Although iSALE-3D simulation results show good agreement with normal-incidence crater scaling laws in strengthless and frictional targets (Elbeshausen et al. 2009), the code has not yet been tested against laboratory experiments of oblique impact.

For any computational model, it is important to have confidence in the results the model produces. Codes need to be thoroughly tested before they can be used to simulate scenarios that cannot be observed by any other method (Pierazzo et al. 2008). Validation is a form of testing in which model output is compared with experimental results to demonstrate that the model can reproduce reality within some error criteria. To properly validate a code, a well-documented set of experimental data is required, so that the initial conditions can be replicated in the model. For example, Hayhurst et al. (1995) validated the hydrocode AUTODYN-3D against the experimental results of Christiansen et al. (1993). Herein, we conduct a similar validation exercise in which we compare iSALE-3D results against the experimental results of Burchell and Mackay (1998). In the experiments whose geometry we replicate in our model, an aluminum target was impacted by aluminum projectiles at a range of impact angles using a horizontal two-stage light-gas gun. This experimental data set was chosen for several reasons. Most pertinently, direct access to these experimental results allowed us to construct new measurements of crater shape and crater dimensions. In addition, the high strength of aluminum and the horizontal orientation of the gun imply that crater growth is limited by target strength, rather than gravity. Hence, gravitational forces can be neglected and, more importantly, the final crater size is limited to several impactor radii, which is computationally less challenging to simulate than a crater formed in a weak material that grows to be many times the size of the impactor. An additional advantage of validating iSALE-3D against this set of data is that the same material can be used for both the projectile and the target surface, which saves on computational resources.

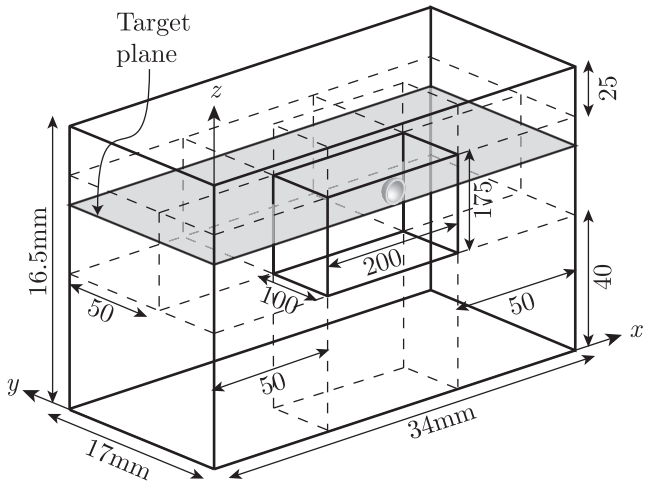

Fig. 1. Sample iSALE-3D computational mesh used for calculating impacts into aluminum with shear strength of 200 MPa at a resolution of 12 cppr. The inner solid line shows the high-resolution zone of $200 \times 100 \times 175$ cells. Dashed lines show the extension zone, where the edge of each cell moving away from the high-resolution zone is 6% longer than the previous extension cell. Measurements are given in numbers of cells, except where noted. The target plane is shown in gray.

To reproduce the experiments numerically, a computational mesh was constructed as a half space, with a symmetry plane down the center of the projectile, along the horizontal component of the velocity of the projectile. This half-space geometry allows a larger mesh to be used (and hence a higher resolution) compared with modeling the entire domain. The mesh had a high-resolution zone close to the impact site, which was approximately $200 \times 100 \times 175$ cells in size in the x, y, and z coordinates, respectively (see Fig. 1). In each coordinate direction, a set of "extension" cells was used to mitigate reflections of the shock wave from the mesh boundaries interacting with the impact site. Fifty extension cells were used in the x- and y-directions, 40 cells at the bottom of the mesh, and 25 at the top, where each extension cell had an edge length 6% larger than its inner neighbor moving away from the high-resolution zone. The experiments were performed onto aluminum disks many times larger than the crater (approximately 10 cm in diameter and approximately 1 cm thick), and so it is expected that shock reflections did not play an important role in either the experiments or the simulated craters. The symmetry plane in the model was in the x–z plane, and so the extension cells in the y-direction were only applied on one side of the mesh (opposite the symmetry plane), whereas in the x-direction the extension zone was applied at both sides of the mesh. The boundary condition on the top of the mesh allowed

Table 2. Material parameters for aluminum used in this study.

Parameter	Value
Poisson ratio	0.35
Shear strength (Y_0)	200 MPa/20 MPa/2 MPa
Melt temperature	660 K
Specific heat capacity	900 J/(kg K)
Tillotson parameters	
Density	2700 kg m^{-3}
a	0.5
b	1.63
A	75.2 GPa
B	65 GPa
E_0	5.0 MJ kg^{-1}
α	5
β	5
E_{iv}	3.0 MJ kg^{-1}
E_{cv}	13.9 MJ kg^{-1}

Three different values of shear strength are used (see the Results II—Effect of Target Strength section) to test the effect of material strength on crater morphology. All other parameters are kept the same. The Tillotson parameters presented here are taken from Melosh (1989).

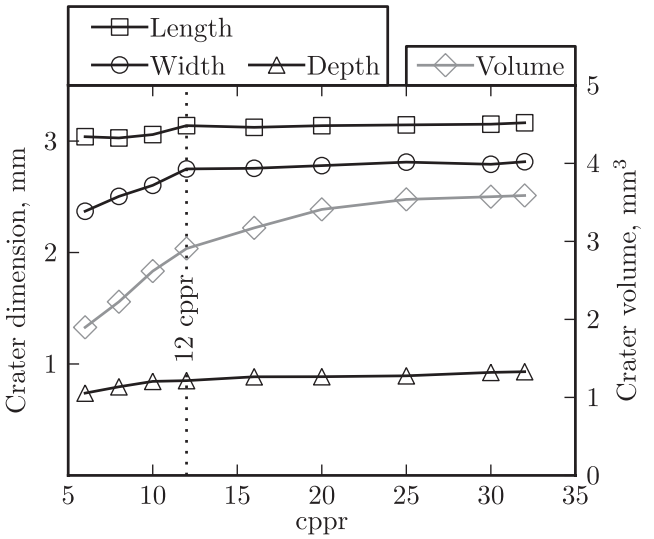

Fig. 2. Resolution study for an impact of a 1 mm diameter aluminum sphere at 5 km s^{-1} and $\theta = 30°$ into aluminum with 200 MPa shear strength. Resolution is measured in cells per projectile radius (cppr). Note the different *y*-axes for diameter and depth measurements and crater volume. This plot shows that at low resolution (< 12 cppr), the crater dimensions are underestimated. However, above a resolution of approximately 12 cells per projectile radius (cppr), the error due to resolution is small for measurements of *L*, *W*, and *D*. The measurement of crater volume is more sensitive to the resolution used.

continuous outflow of material; the bottom of the mesh had a no-slip boundary condition (zero velocity at the boundary); all other boundaries had a free-slip boundary condition (zero velocity normal to the boundary). The initial condition assigned a velocity toward the target (at the required impact angle) to all cells in the projectile, and zero velocity throughout the target. Time = 0 was defined as the instant that the projectile made first contact with the target material.

The impactor and target material was simulated using the well-established Tillotson equation of state (Tillotson 1962) with parameters for aluminum. Material strength was modeled using a von Mises yield criterion with a shear strength (Y_0) of 200 MPa, together with a simple thermal softening model (Ohnaka 1995; Collins et al. 2004). This strength model was chosen as the simplest model that produced a good match to experimental results in a previous validation exercise (Pierazzo et al. 2008), and measurements of the shear strength of aluminum (e.g., Parker 1967). Material parameters employed in the model can be found in Table 2.

Simulations were run with a resolution of 12 cells per projectile radius (cppr). To confirm that this resolution was sufficient to adequately simulate these oblique impact angle cratering events, simulations were run at different resolutions (between 6 cppr and 32 cppr) for an impact angle of 30°. Crater dimensions for each resolution are presented in Fig. 2. Below 12 cppr, iSALE-3D underestimates the dimensions of the crater. However, for 12 cppr and above (i.e., 16–32 cppr), there is very little difference in the measured crater dimensions. Crater length, width, and depth are 0.8%, 2.3%, and 8.6% smaller at 12 cppr than at 32 cppr, respectively. Crater volume is 18.9% smaller at 12 cppr than at 32 cppr. In previous work using iSALE-3D, Elbeshausen et al. (2009) found that this inaccuracy is slightly scale-dependent. Using a resolution of 8 cppr for large planetary-scale impacts (a projectile size of 250 m and impact velocity of 6.5 km s^{-1}), they found the measurements at $\theta = 90°$ for crater diameter, depth, and volume to be 6.3%, 2.8%, and 12% too small, respectively, compared with the projected dimension at "infinite" resolution.

To produce a comparable data set to the laboratory experiments, simulations were performed with a range of impact angles from perpendicular to the target plane (90°) to 10° from the horizontal. The impact velocity was kept constant at 5 km s^{-1} (the average velocity in the laboratory experiments), and the impactor was modeled as a sphere with a diameter of 1 mm in all simulations.

To investigate the effect of target strength on the relationship between impact angle and crater size and shape, simulations were also performed for lower strength targets. The shear strength of the aluminum was reduced to 20 MPa and 2 MPa. In these simulations, a larger computational mesh and a slightly lower resolution (10 cppr) were employed to accommodate the larger craters formed in weaker targets. Due to the extra

computational expense of the larger mesh, simulations with a 2 MPa shear strength were only run for impact angles necessary to determine the elliptical crater threshold angle. Simulations were completed when crater growth had ceased and the crater rim rollover had stopped.

QUANTIFYING LAB-SCALE EXPERIMENTAL WORK

To accurately compare the iSALE-3D results with the experimental work, a digital elevation model (DEM) for each of the aluminum craters formed in the laboratory was constructed. Using a JEOL JSM-5900LV scanning electron microscope (SEM), a stereo-pair of images of the crater were taken with a difference in viewing angle of 6°. Image processing software (MeX from Alicona) was used to construct the DEM (e.g., Kearsley et al. 2007, 2008), allowing for measurements to be taken of the crater relative to the ambient target plane. The resolution of the DEM was approximately 3 μm per grid square. From this DEM, profiles were drawn through the crater in both the direction parallel to the impact trajectory (along the longest diameter of the crater) and perpendicular to the impact trajectory (at the maximum diameter in this orientation). Data were also extracted from the DEM to construct an outline of the shape of the crater at the pre-impact target surface. These profiles and planforms can be seen in Figs. 3 and 4. Measurements were taken of the length, L (the diameter in the direction parallel to the trajectory of the impactor, at the ambient plane); the width, W (the maximum diameter perpendicular to the crater length, at the ambient plane); the maximum depth, D, of the crater; and the offset of the deepest point from the center of the crater along range, O (see Table 3 and Figs. 5 and 6). The mean error between the DEM measurement and the original measurements was 6.0%, with a standard deviation of 5%. It is important to note here that the discussion below on the length of the crater refers to the diameter of the primary crater measured at the pre-impact target plane, and not at the total damage length. The volume of the crater was calculated by summing the volume for each grid square of the DEM between the crater floor and the ambient plane (see Fig. 7).

RESULTS I—VALIDATION

Crater Dimensions

Measurements of crater volumes and dimensions (see Fig. 5 for definitions) were also extracted from the simulations (see the measurements for aluminum with a shear strength of 200 MPa in Figs. 6 and 7 and Table 3). The measurements of volume V, length L, width W, and depth D on Figs. 6 and 7 are normalized by the corresponding dimension of the simulated crater formed at 90° to the target plane (e.g., crater volume $V_\perp$). The experimental data was normalized by the mean of the dimensions of the craters formed by impacts at 80° and 90°. This was to account for the fact that crater formed at 90° was anomalous, being smaller (in length, width, depth, and volume) than the crater formed at 80°. Possible explanations for this anomaly include target inhomogeneities or variations in the projectile diameter (M. Burchell, personal communication). By normalizing all the crater measurements, direct comparison between the experimental and simulated craters for a range of target materials and strengths is possible (see the Results II—Effect of Target Strength section). From these data, the characteristic cratering efficiency for each target type can be found. Herein, we define the vertical impact cratering efficiency, $\pi_\perp = L_\perp/d_p$, as the diameter of the crater formed by impact at 90° to the target plane divided by the projectile diameter (d_p, 1 mm in all cases here). For both the experiment and the iSALE-3D crater with $Y_0 = 200$ MPa, $\pi_\perp \approx 3.5$.

The volume of the simulated craters agrees well with the measurements taken from the DEM's of the Burchell and Mackay (1998) aluminum craters, and the craters formed in granite targets from the laboratory work of Gault and Wedekind (1978)—note that a normalized measurement of crater volume is comparable to a normalized measurement of displaced mass. All of these data sets can be approximated by:

$$V(\theta)/V_\perp = \sin^2(\theta) \quad (2)$$

at angles $< 30°$, and lie between $\sin(\theta)$ and $\sin^2(\theta)$ for angles $> 30°$ (see Fig. 7). The best fit for the simulated craters with $Y_0 = 200$ MPa is $V(\theta)/V_\perp = \sin^n(\theta)$, where $n = 1.6$, with a goodness of fit of $R^2 = 0.988$.

The simulated crater dimensions are a good fit to the experimental measurements of both crater width and depth at all impact angles (Figs. 6b and 6c and Table 3). The crater depth varies linearly with the sine of the impact angle (with a goodness of fit to the $Y_0 = 200$ MPa data of $R^2 = 0.984$) i.e.,

$$D(\theta)/D_\perp = \sin(\theta) \quad (3)$$

The crater width measurements are well fit by the function:

$$W(\theta)/W_\perp = \sin^{0.46}(\theta) \quad (4)$$

for which the goodness of fit, $R^2 = 0.925$. This function slightly overestimates the crater width at very oblique impact angles ($< 20°$).

In the iSALE-3D simulations, the crater length decreases at lower incidence angles (Fig. 6a). For

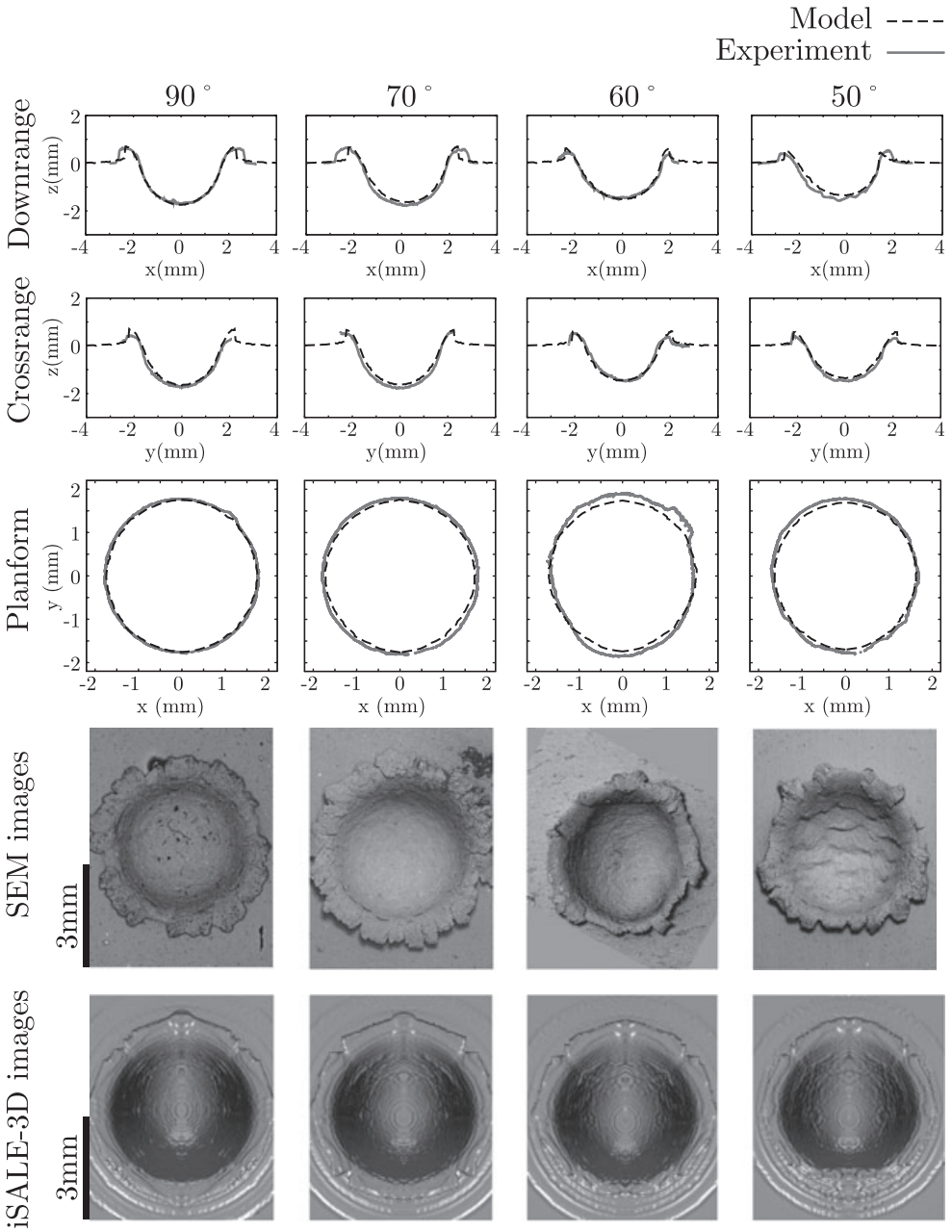

Fig. 3. Profiles and planforms of craters from the experiments of Burchell and Mackay (1998) (using DEM's generated from SEM image pair) and iSALE-3D for 200 MPa shear strength aluminum, for impact angles 90–50°. Profiles are drawn downrange (parallel to the horizontal component of velocity—the downrange direction is to the left) and crossrange (perpendicular to the horizontal component of velocity). Planforms are drawn at the pre-impact target surface elevation, measured from the center of the crater outwards. For all plan views and SEM images, the downrange direction is up the page.

example, the normalized length of the crater formed with $\theta = 30°$ is 0.89. At $\theta = 20°$, the length decreases to 0.79. These simulations can be approximated by the function:

$$L(\theta)/L_{\perp} = \sin^{m}(\theta), \tag{5}$$

where $m = 0.22$ and $R^2 = 0.976$. However, the laboratory experiments do not exhibit the same monotonic decrease in crater length with decreasing impact angle. With the exception of the crater with an incidence angle of 20°, all experimental craters in aluminum for which a DEM has been constructed have a length within 5% of the normal-incidence crater. Even the crater for which $\theta = 20°$ is only 12% smaller than the normal-incidence crater (compared with the 21% reduction in length for the iSALE-3D simulation).

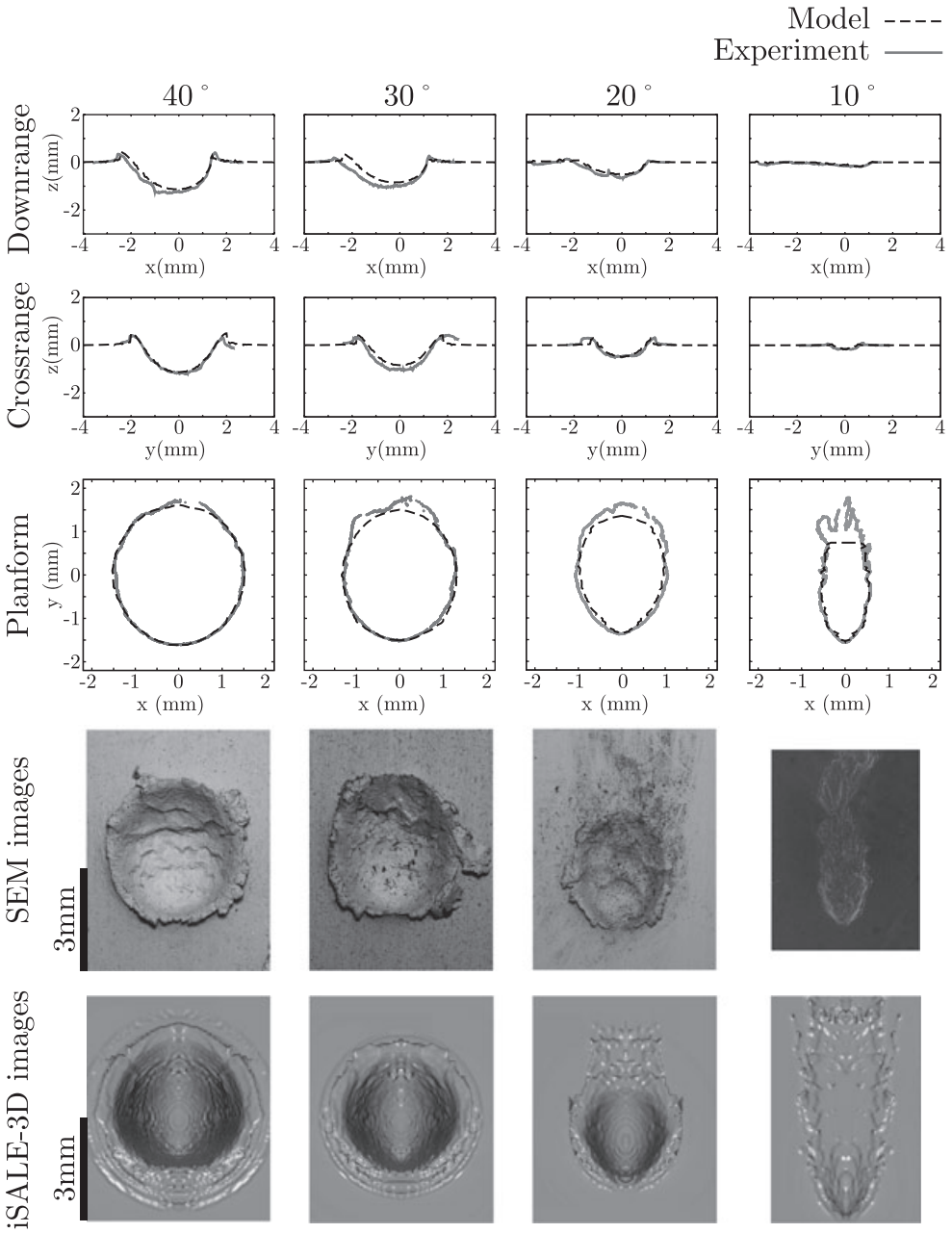

Fig. 4. As Fig. 3, but for angles 40–10°. Planforms for craters with impact angles of 10° and 20° show only the primary crater; additional damage, caused by the projectile plowing into the surface downrange of the main crater, is not shown.

The two laboratory craters with $\theta = 10°$ and $\theta = 30°$ (see Fig. 6a) are both much longer than would be expected from the simulations (if the trend for length to decrease at low angle is correct). The $\theta = 30°$ crater has a normalized length of 1.04 measured from the DEM (the equivalent measurement in Burchell and Mackay (1998) is 1.02). The $\theta = 10°$ crater has a normalized length of 0.97 from both the DEM measurement and Burchell and Mackay (1998). A possible explanation for the additional length of these two craters is that in measuring the length, extra downrange damage (e.g., secondary crater pits possibly caused by a "decapitated" projectile) is being taken into account, artificially lengthening the craters. This damage may be recorded in the high-resolution DEM of the crater, but is not simulated in iSALE-3D. A higher resolution simulation (25 cppr) is presented in Fig. 8, which shows the decapitation of the projectile, and additional damage occurring due to the projectile plowing into the target surface downrange of the main crater. It is possible that if these downrange craters were close enough

Table 3. Crater dimensions from laboratory and numerical modeling work.

Angle	DEM measurements aluminum					iSALE-3D 200 MPa					iSALE-3D 20 MPa					iSALE-3D 2 MPa				
(°)	*L*	*W*	*D*	*O*	*V*	*L*	*W*	*D*	*O*	*V*	*L*	*W*	*D*	*O*	*V*	*L*	*W*	*D*	*O*	*V*
90	3.50	3.47	1.73	0.50	10.4	3.51	3.48	1.75	0.51	9.55	6.35	6.35	3.15	0.50	56.7	11.9	11.8	5.60	0.50	674
80	3.63	3.66	1.94	0.43	12.1						6.35	6.33	3.11	0.52	55.5					
70	3.61	3.58	1.79	0.47	10.5	3.54	3.50	1.63	0.46	8.84	6.23	6.24	3.02	0.51	52.3					
60	3.68	3.22	1.51	0.50	8.70	3.48	3.42	1.53	0.45	7.87	6.07	6.06	2.86	0.49	46.8					
50	3.55	3.30	1.57	0.48	8.22	3.38	3.33	1.37	0.44	6.58	5.78	5.74	2.65	0.48	38.9					
40	3.46	3.18	1.31	0.52	4.83	3.20	3.06	1.13	0.45	4.81	5.33	5.30	2.30	0.50	28.8					
35						3.15	2.89	0.99	0.43	3.78										
30	3.63	2.86	1.04	0.47	4.15	3.14	2.75	0.85	0.46	2.95	4.62	4.57	1.85	0.49	17.4					
20	3.06	2.09	0.64	0.33	1.44	2.77	2.21	0.50	0.33	1.09	3.78	3.45	1.25	0.43	6.97	6.30	6.26	2.66	0.48	46.0
15						2.52	1.62	0.33	0.35	0.49	3.40	2.72	0.89	0.37	3.29	4.92	4.93	2.00	0.49	21.7
10	3.38	1.25	0.19	0.15	0.16	2.41	1.17	0.17	0.29	0.15	3.26	1.91	0.55	0.33	1.11	4.37	3.41	1.30	0.37	7.58
5											1.90	1.30	0.25	0.28	0.17					

Dimensions of craters formed in the laboratory (Burchell and Mackay 1998—figures shown here are the measurements taken from the DEM created from the SEM image pair) and simulated with iSALE-3D at a range of shear strengths.
Columns are L = Length; W = width; D = maximum depth; O = offset; V = volume (see Fig. 5 for definitions of these measurements). L, W, and D are in mm; V is in mm^3.

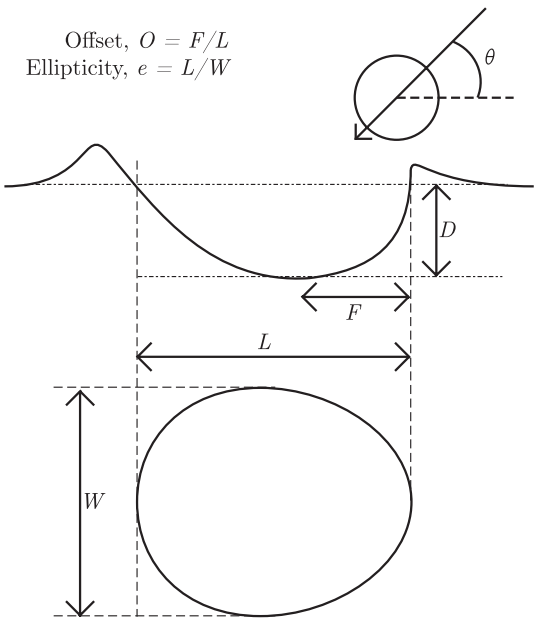

Fig. 5. Dimensions used to quantify the size and asymmetry of a crater. The diameter of the crater is taken at the pre-impact target surface, and can be broken into two components—the length of the crater, L, in the direction of the horizontal velocity component and the width of the crater, W, in the direction perpendicular to the horizontal movement. The ellipticity of the crater, as defined in Bottke et al. (2000) is the length divided by the width ($e = L/W$). The depth of the crater, D, is measured from the pre-impact target surface to the deepest point. The offset of the deepest point, O, can be characterized by the ratio of the distance to the deepest point from the up-range wall of the crater to the length of the crater.

to the main crater to join up with it, the DEM measurements would include them and artificially lengthen the crater measurement.

Crater Shape

To further validate iSALE-3D against the experiments of Burchell and Mackay (1998), along- and cross-range profiles of the simulated craters have been superimposed upon the equivalent profiles drawn from the DEM's of the experiments (see Figs. 3 and 4). iSALE-3D results are an excellent match to the crater shape and the along-range profile asymmetry at all impacts angles (i.e., the steeper angle of the uprange wall, the shallower angle of the downrange wall, and the offset of the deepest point toward the uprange wall). Also shown in Figs. 3 and 4 are planforms of the crater shape drawn at the ambient plane. Again, the simulated craters show very close agreement in shape and size to the experiments. In some craters (i.e., $\theta < 30°$), the experiments show some extra downrange damage, possibly from a decapitated projectile (see Burchell and Mackay 1998 and Fig. 8).

The offset of the deepest point from the uprange wall of the crater, O, for the iSALE-3D simulations fits the experimental data well (Fig. 6d). At angles greater than 30° from the horizontal, the deepest point is approximately midway between the uprange and downrange walls ($O \sim 0.5$). At more oblique angles ($\theta < 30°$), the deepest point is offset toward the uprange wall ($O < 0.5$), consistent with the observation that the uprange wall is steeper than the downrange wall. At 10°, the deepest point observed in the experimental crater ($O = 0.15$) is offset from the center more than in the iSALE-3D simulation ($O \sim 0.3$). However, the crater formed at this impact angle is very shallow, and therefore measuring the length and depth is highly

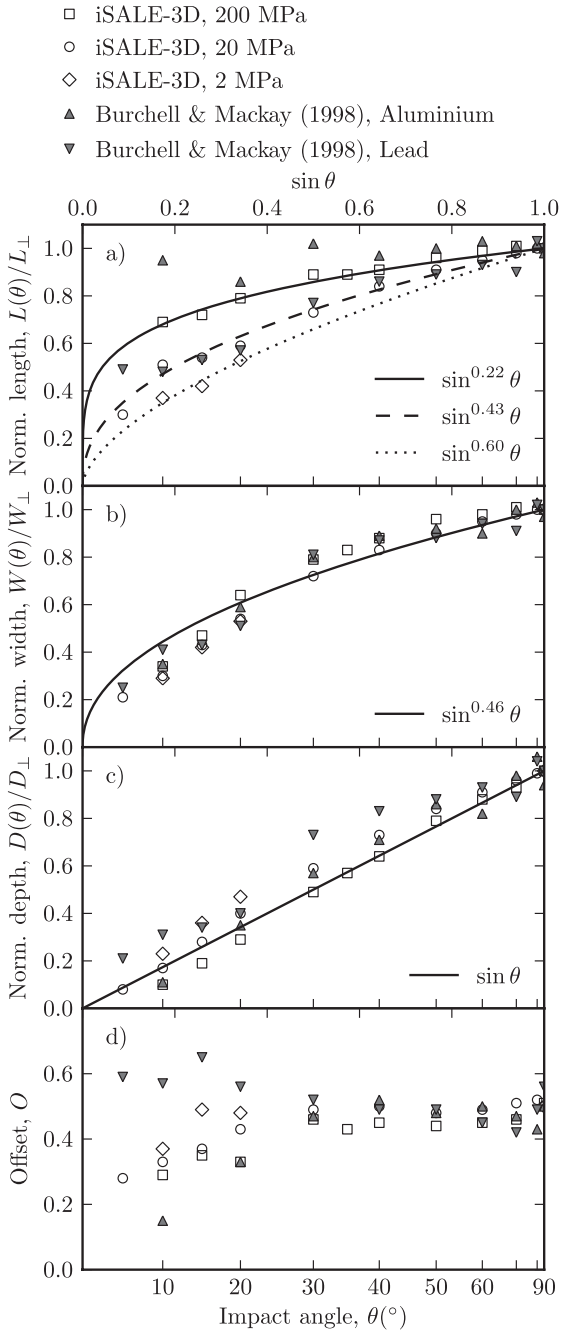

Fig. 6. Dimensions of craters formed in the experimental work of Burchell and Mackay (1998) and for iSALE-3D craters in each target strength. a) Normalized crater length. The three sine functions are fit to each simulated target strength (see text for details). b) Normalized crater width. The simulated craters with a shear strength of 200 MPa are fit well by $W(\theta)/W_{\perp} = \sin^{0.46}(\theta)$. c) Normalized maximum depth of the crater, measured from the pre-impact target plane. These measurements are fit well by $D(\theta)/D_{\perp} = \sin(\theta)$. d) Offset of the deepest point, O, from the uprange wall of the crater. As a result of the anomalously small crater formed at $\theta = 90°$, the experimental results for length, width, and depth have all been normalized by the average of the dimensions from the $\theta = 90°$ and $\theta = 80°$ craters.

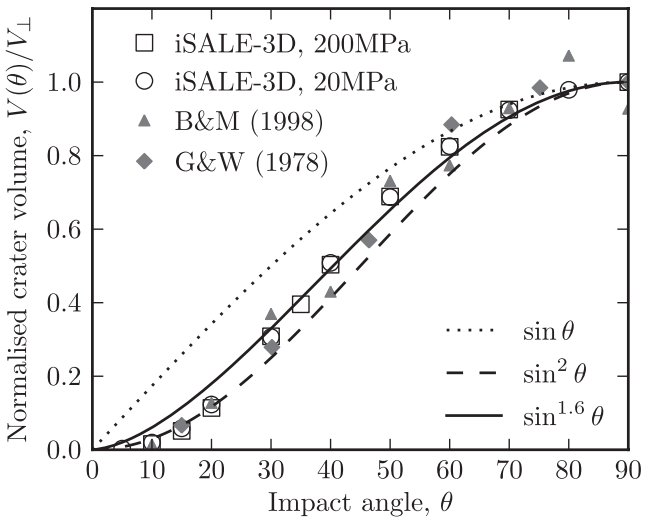

Fig. 7. Crater volumes normalized to the crater volume formed when the impact angle is perpendicular to the target surface. Results shown are for iSALE-3D simulations for the two different strengths of aluminum, and laboratory experiments into granite targets from Gault and Wedekind (1978) and aluminum targets from Burchell and Mackay (1998). The best fit line of $\sin^{1.6}(\theta)$ is fit to the simulated craters from iSALE-3D with a shear strength of 200 MPa (open squares). Note that the Burchell and Mackay (1998) aluminum crater volumes are normalized by the average of the dimensions from the $\theta = 90°$ and $\theta = 80°$ craters (see text for details).

dependent on the resolution used in the modeling and the construction of the DEM. Also, the length of the experimental crater was measured to be 3.38 mm (only 0.12 mm shorter than the normal-incidence crater), which may be artificially lengthened by some additional damage downrange that is not modeled as part of the primary crater. This would have the effect of offsetting the deepest point to be relatively closer to the uprange wall.

Table 4 and Fig. 9 show the calculated crater ellipticity ($e = L/W$; see the Crater Shape section for discussion of the measurement of crater length and width) for the simulated and experimental craters. By defining an elliptical crater as a crater with ellipticity $e > 1.1$ (Schultz and Lutz-Garihan 1982), comparisons can be drawn between the simulations and experiments. For the Burchell and Mackay (1998) aluminum craters measured using the SEM techniques, the threshold angle (θ_e) between circular and elliptical cratering behavior is 30–40°. This is consistent with the simulated craters, for which $\theta_e = 30–35°$.

The simulations presented above with $Y_0 = 200$ MPa in general show good agreement with both the crater dimensions and the crater shape parameters measured from the laboratory experiments. Following the successful validation of the model, the Results

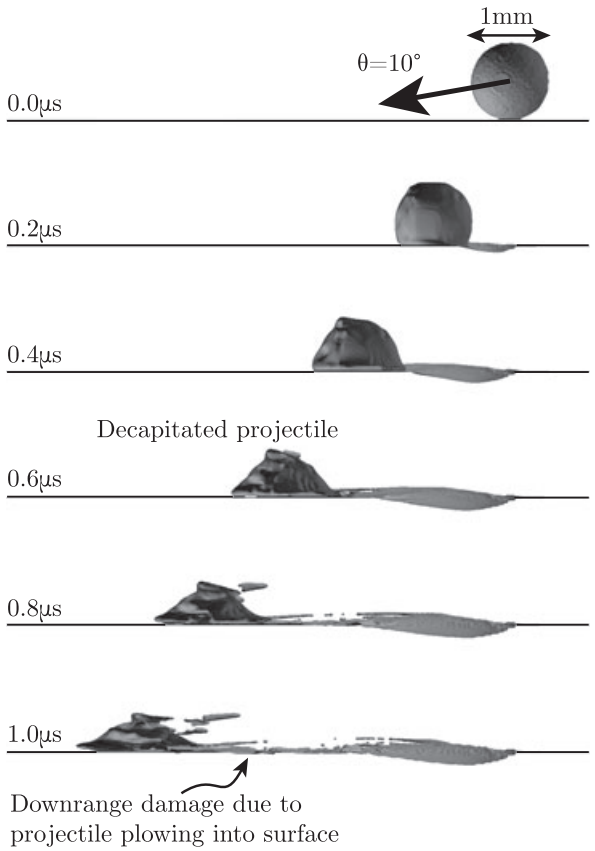

Fig. 8. Snapshots from an iSALE-3D simulation at several times in the cratering process for a $\theta = 10°$ impact. Resolution is 25 cppr. By 0.6 μs, the projectile has been decapitated, and causes further damage to the surface downrange of the main crater.

II—Effect of Target Strength section presents a study of the effect of changing target strength on crater size and shape for a range of impact angles.

RESULTS II—EFFECT OF TARGET STRENGTH

To investigate the role of target strength on oblique crater formation, two additional suites of simulations at various impact angles were performed, with target shear strengths $Y_0 = 20$ MPa and 2 MPa, respectively. The same equation of state for aluminum was used as in the previous set of simulations. Results from simulations are shown in Tables 3 and 4 and Figs. 6, 7, and 9. By reducing the shear strength to 20 MPa and 2 MPa, the vertical impact cratering efficiency $\pi_\perp$ is increased from 3.5 to 6.4 and 11.8, respectively. In this sense, simulations with a shear strength of 20 MPa are roughly comparable to impact experiments from Burchell and Mackay (1998) with steel ($\rho_p = 7930$ kg m^{-3}) projectiles impacting into lead targets ($\rho_t = 11{,}340$ kg m^{-3}) that have a cratering efficiency of 7.0, although it must be noted that the simulations have $\rho_p = \rho_t$, whereas the experiments with lead targets have $\rho_p < \rho_t$. The shear strength of lead is approximately an order of magnitude lower than that for aluminum (a range of strength values are reported for different compositions of lead; typical values are approximately 10–15 MPa; Parker 1967; International Nickel Company, 1968).

Effect of Target Strength on Crater Size

For all target strengths, the crater length decreases as the impact angle decreases. However, the reduction in crater size with decreasing impact angle is more pronounced in weaker targets. For example, at an impact angle of 20°, the length of the simulated crater is 0.8 times the vertical impact crater diameter for $Y_0 = 200$ MPa; this ratio drops to 0.6 for $Y_0 = 20$ MPa, and 0.53 for $Y_0 = 2$ MPa. Also, note that the normalized crater length of the $Y_0 = 20$ MPa simulations matches closely with the equivalent data from the lead-target experiments. The decrease in length with increasing obliquity can be approximated by Equation 5; for $Y_0 = 20$ MPa, $m = 0.43$ (and $R^2 = 0.988$), and for $Y_0 = 2$ MPa, $m = 0.60$ (and $R^2 = 0.996$).

The shear strength of the target material has no effect on the decrease in crater width with decreasing crater angle. Equation 4, which was fitted to results from simulations with $Y_0 = 200$ MPa, also fits well both sets of simulations with lower shear strength and the impact experiments with lead targets (see Fig. 6).

Reducing the target material strength has the effect of increasing crater depth at low impact angles. Simulated craters with $Y_0 = 200$ MPa plot on or below the line $D(\theta)/D_\perp = \sin(\theta)$ for all angles $\theta < 40°$. However, for simulations with $Y_0 = 20$ MPa, all points are on or above that line, and for $Y_0 = 2$ MPa, the three simulated craters at $\theta = 10°$, 15°, and 20° are all deeper than $D_\perp \sin(\theta)$. The impact experiments with lead targets are also deeper than the $\sin(\theta)$ line, although as noted in Burchell and Mackay (1998), when $\rho_p < \rho_t$, the normalized depth measurements are best fit by $\sin^b(\theta)$. They show two cases where $\rho_p < \rho_t$. For cellulose acetate projectiles impacting aluminum targets, $b > 1$ (and hence the craters are less deep). However, for the steel projectiles impacting lead targets, they find that $b < 1$. Clearly, more work is needed to understand the complex relationship between ρ_p/ρ_t and crater depth.

Effect of Target Strength on Crater Shape

Asymmetry in the simulated crater shape was quantified by e, the crater ellipticity (L/W) and O, the offset (along the direction of impact) of the deepest point of the crater from its center. Both of these measures show an abrupt change below a critical threshold angle.

Table 4. Ellipticity of laboratory and simulated craters.

Angle (°)	Experiment—Aluminum	Experiment—Lead	iSALE-3D—200 MPa	iSALE-3D—20 MPa	iSALE-3D—2 MPa
90	1.01	1.01	1.01	1.00	1.00
80	0.99	1.02		1.00	
70	1.01	1.01	1.01	1.00	
60	1.14	1.00	1.02	1.00	
50	1.08	1.03	1.01	1.01	
40	1.09	1.00	1.05	1.01	
35			1.09		
30	**1.27**	0.97	**1.14**	1.01	
20	1.46	**1.15**	1.26	1.09	1.01
15		1.27	1.56	**1.25**	1.00
10	2.71	1.20	2.07	1.71	**1.28**
5		1.94		1.46	

Ellipticity ($e = W/D$) of craters formed in the laboratory by Burchell and Mackay (1998) and simulated with iSALE-3D at a range of shear strengths. The figures shown here for aluminum are the measurements taken from the DEM created from the SEM image pair, and for lead are the measurements made by Burchell and Mackay (1998). Figures in bold type show the least oblique impact angle for which an elliptical crater ($e > 1.1$) is formed.

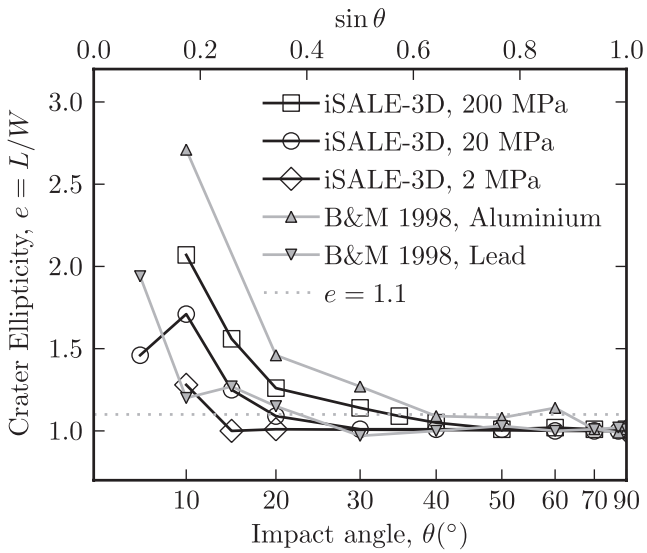

Fig. 9. Ellipticity ($e = L/W$) of craters from Burchell and Mackay (1998) and iSALE-3D. Note that the transition from circular to elliptical is for impact angles 30–40° for the Burchell and Mackay (1998) aluminum experiments and iSALE-3D with a strength of 200 MPa. For iSALE-3D with shear strength of 20 MPa and the impact experiments into lead, the transition to elliptical craters occurs at approximately 20°. For $Y_0 = 2$ MPa, $\theta_\varepsilon = 10$–15°.

At high angles, the crater is circular ($e < 1.1$), and the deepest point is equidistant between the downrange and uprange crater rim ($O \approx 0.5$); at low angles, the crater is elliptical ($e > 1.1$) and the offset of the deepest point is toward the uprange wall ($O < 0.5$). The asymmetry of the crater is more extreme at shallower impact angles. In the experiments into lead targets, the offset is toward the downrange wall ($O > 0.5$), which may suggest a role of projectile/target density ratio.

The threshold angle below which asymmetric craters are formed decreases with decreasing target strength. For $Y_0 = 200$ MPa, the elliptical crater threshold angle $\theta_e = 30$–35°; for $Y_0 = 20$ MPa, $\theta_\varepsilon = 15$–20°; and for $Y_0 = 2$ MPa, $\theta_\varepsilon = 10$–15°. Similarly, the crater offset O drops below 0.4 at angles below 30°, 20°, and 10° for target strengths of 200 MPa, 20 MPa, and 2 MPa, respectively. In the laboratory craters formed in lead targets, $\theta_\varepsilon \approx 20°$, similar to the simulated case, where $Y_0 = 20$ MPa.

DISCUSSION

Pi-Group Scaling in Vertical and Oblique Impacts

Scaling laws are often used to extrapolate small-scale laboratory experiments to larger scales. One such suite of equations for vertical impacts, the so-called Pi-group scaling laws (e.g., Holsapple and Schmidt 1982, 1987; Holsapple 1987; Schmidt and Housen 1987) are used to predict crater dimensions in terms of projectile and target properties. Pi-group scaling introduces three dimensionless independent variables: the gravity-scaled size ($\pi_2 = gL/U^2$, where g is gravity, L is the impactor diameter, and U is the impact velocity); the strength-scaled size ($\pi_3 = Y/\rho_p U^2$, where Y is the target strength and ρ_p is the projectile density); and the impactor-target density ratio ($\pi_4 = \rho_t/\rho_p$, where ρ_t is the target density). A dimensionless measure of the crater volume, π_V, can be described by a functional relationship of these three quantities:

$$\pi_V = \rho_t V/m = F(\pi_2, \pi_3, \pi_4), \quad (6)$$

where m is the impactor mass and V is the crater volume. For craters in the strength regime (i.e., where the effect of gravity is negligible, as in the cases simulated in this work),

π_2 is negligible. Furthermore, if the target and projectile densities are equal, π_V can be expressed as a power law function of π_3 alone (Schmidt and Housen 1987):

$$\pi_V = C_V \pi_3^{-\gamma}, \quad (7)$$

where C_V and γ are material dependent scaling parameters.

To modify Pi-group scaling laws for oblique impacts, Chapman and McKinnon (1986) suggested that the impact speed (U), which appears in the equation for the strength (or gravity) scaled impactor size, be replaced by the vertical component of the velocity vector $U \sin \theta$. With this modification, Equation 7 becomes:

$$\pi_V = C_V \left(\frac{Y}{\rho_t (\sin(\theta) \cdot U)^2} \right)^{-\gamma} = C_V \left(\frac{Y}{\rho_t U^2} \right)^{-\gamma} \sin^{2\gamma}(\theta) \quad (8)$$

which implies that $V(\theta)/V_\perp = \sin^{2\gamma}(\theta)$.

To test whether the prediction of Chapman and McKinnon (1986) is supported by our numerical model results, we analyzed the outcome of vertical impact simulations where the target shear strength varied between 2 and 200 MPa and the impact velocity between 1.25 and 20 km s^{-1} to estimate the exponent γ in Equation 4. The volumetric cratering efficiency π_V is plotted as a function of π_3 for these simulations in Fig. 10. A power law fit to the data is also plotted, according to Equation 7; the goodness of fit $R^2 = 0.995$, and the scaling constants are $C_V = 0.187$ and $\gamma = 0.79$. If Equation 8 applies, this would predict that crater volume, normalized by the volume of the crater in a vertical impact, scales as $\sin^{1.58}(\theta)$. Hence, our oblique impact simulation results, which are best fit by the expression $V(\theta)/V_\perp = \sin^{1.6}(\theta)$, support the concept that Pi-group scaling can be modified by replacing the impact velocity with the vertical component of the impact velocity for strong ductile target materials. Elbeshausen et al. (2009) showed that this assumption does not hold for materials with no or little cohesion, such as sand.

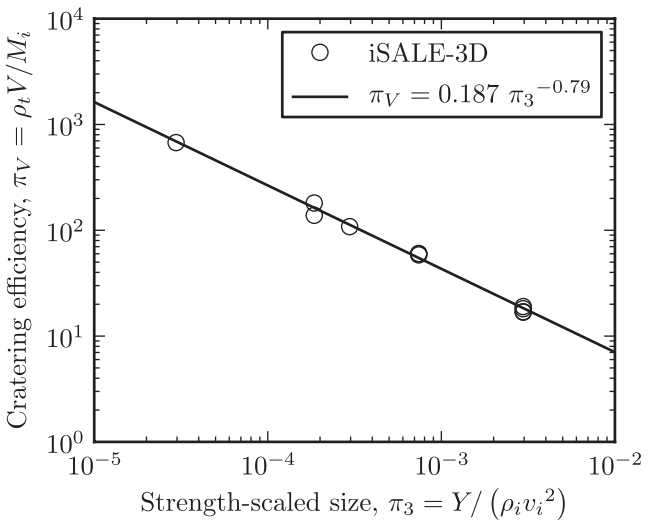

Fig. 10. Cratering efficiency as a function of the strength-scaled size. Several iSALE-3D simulations are shown with $\theta = 90°$ and a variety of strength and impactor velocities. A power law is fit to these data according to Equation 4, with $R^2 = 0.995$; $C_V = 0.187$, and $\gamma = 0.79$.

Applicability to Impacts on Planets and Other Cosmic Bodies

The simulations presented here considered a simple ductile target material with pressure- and strain-independent shear strength, and used an impact velocity (5 km s^{-1}) somewhat lower than is typical for planetary impacts. Further work using higher impact velocities and target strength models that more accurately represent the response of planetary surfaces to impact is warranted to fully understand how impact obliquity affects crater morphology in nature (e.g., Collins et al. 2011). However, the cratering efficiencies for our impact simulations with target shear strength of 2–20 MPa are comparable to estimates of the efficiency of planetary-scale impact events from Pi-group crater scaling laws (Holsapple 1993). Moreover, the shear strength model used in these simulations is similar to the estimates of the effective strength of a planetary surface at the simple-to-complex transition (approximately 3 MPa with very low internal friction angle; e.g., Melosh and Ivanov 1999), albeit without the effects of gravity included. We also note that in our simulations which assumed a target shear strength of 2 MPa, the threshold angle for elliptical crater formation was 10–15°, which is consistent with the observed fraction of elliptical craters on the Moon, Mars, and Venus (e.g., Schultz and Lutz-Garihan 1982; Bottke et al. 2000). Therefore, although the quantitative results of this work must be extrapolated to the planetary scale with great caution, many of the qualitative observations, and some of the quantitative trends, established by this work regarding the effect of impact obliquity on crater size and morphology may well be applicable to larger scale impact events.

The formation of an impact crater on a small cosmic body with low gravity is likely to be controlled by the material strength rather than the gravity of the target body (strength-dominated cratering). Therefore, many of the results presented above for impacts into strong targets could be applied to this type of impact event. However, two additional processes must be considered: First, the process of spallation, which was not considered in our plastic strength model, dominates impacts on rocky targets at small scales. Second, small bodies such as asteroids are likely to contain a significant proportion of pore space (e.g., Britt et al. 2002). Porosity is well known to affect the cratering process (e.g., Love et al. 1993; Housen and Holsapple 2003) and so further three-

dimensional modeling, with the inclusion of a model to account for porous compaction and spallation during the impact is necessary to truly extrapolate these results to small body impacts.

Another scenario in which the cratering process is controlled by the target material strength is the impact of space debris on the surface of spacecraft. Strong, ductile materials, such as aluminum, are often used in spacecraft design. In these impact events, gravity is very low and would not affect the crater growth. Therefore, the simulations presented in this study are directly applicable to impacts on spacecraft.

CONCLUSIONS

We have used the iSALE-3D shock physics model to simulate the formation of impact craters on strong, ductile targets at a range of incidence angles. The dimensions of the craters simulated are in good agreement with the dimensions of laboratory-formed craters with an experimental set up being the same as that used in the numerical modeling (Burchell and Mackay 1998). For impact angles less than 30° from the horizontal, the modeling results predict craters that are smaller in length than those formed in the laboratory. However, the experimental craters may be longer due to secondary cratering downrange that merges with the primary crater, and hence appears as an elongated crater. Secondary cratering is not simulated in the model, probably due to a lack of resolution. Other measurements of the width and depth of the simulated craters matched the experimental results well.

iSALE-3D also simulated the change in crater morphology well, as impact angle decreases in all measures used to define the shape: the offset of the deepest point, the slope of the uprange and downrange walls, and the ellipticity of the crater planform. The transition from circular to elliptical craters in the validation simulations occurs at a similar angle to that for craters formed in the laboratory experiments (Burchell and Mackay 1998).

In addition to validating iSALE-3D, we also simulated the formation of oblique impact craters in ductile targets with a range of strengths from 2 MPa to 200 MPa. In a weaker material, the transition from circular to elliptical craters occurs at a lower impact angle. At higher cratering efficiency, the analogy of a point source of momentum and energy is more relevant, and impactor properties such as impact angle play less of a role in influencing crater morphology.

Acknowledgments—We thank Boris Ivanov and Jay Melosh for their work in the development of iSALE and iSALE-3D. We are also very grateful to Mark Burchell for kindly providing us with his experimental targets for reanalysis. We thank Valery Shuvalov and Michael Poelchau for their insightful and helpful reviews. T. M. D. was supported in part by STFC grant ST/G002452/1; G. S. C. was funded by NERC Fellowship grant NE/E013589/1; the contribution to this work by D. E. and K. W. was funded by DFG grant WU 355/5-2 and the Helmholtz Alliance HA-203 "Planetary Evolution and Life."

Editorial Handling—Dr. Natalia Artemieva

REFERENCES

Amsden A. A. and Ruppel H. M. 1981. SALE-3D: A simplified ALE computer program for calculating three-dimensional fluid flow. Los Alamos National Laboratories Report LA-8905.151 p.

Amsden A. A., Ruppel H. M., and Hirt C. W. 1980. SALE: A simplified ALE computer program for fluid flow at all speeds. Los Alamos National Laboratories Report LA-8095.105 p.

Anderson C. E. 1987. An overview of the theory of hydrocodes. *International Journal of Impact Engineering* 5:33–59.

Artemieva N. A. and Ivanov B. A. 2004. Launch of Martian meteorites in oblique impacts. *Icarus* 171:84–101.

Artemieva N. A., Pierazzo E., and Stöffler D. 2002. Numerical modeling of tektite origin in oblique impacts: Implication to Ries-Moldavites strewn field. *Bulletin of the Czech Geological Survey* 77:303–311.

Artemieva N. A., Karp T., and Milkereit B. 2004. Investigating the Lake Bosumtwi impact structure: Insight from numerical modeling. *Geochemistry Geophysics Geosystems* 5:Q11016.

Benson D. J. 1992. Computational methods in Lagrangian and Eulerian hydrocodes. *Computer Methods in Applied Mechanics and Engineering* 99:235–394.

Bottke W. F. Love S. G., Tytell D., and Glotch T. 2000. Interpreting the elliptical crater populations on Mars, Venus, and the Moon. *Icarus* 145:108–121.

Britt D. T., Yeomans D., Housen K., and Consolmagno G. 2002. Asteroid density porosity and structure. In *Asteroids III*, edited by Bottke W. F., Cellino A., Paolicchi P., and Binzel R. Tucson, AZ: The University of Arizona Press. pp. 485–500.

Burchell M. J. and Mackay N. G. 1998. Crater ellipticity in hypervelocity impacts on metals. *Journal of Geophysical Research* 103:22761–22774.

Chapman C. R. and McKinnon W. B. 1986. Cratering of planetary satellites. In *Satellites*, edited by Burns J. A. and Matthews M. S. Tucson, AZ: The University of Arizona Press. pp. 492–580.

Christiansen E. L., Cytowski E. D., and Ortega J. 1993. Highly oblique impacts into thick and thin targets. *International Journal of Impact Engineering* 14:157–168.

Collins G. S., Melosh H. J., and Ivanov B. A. 2004. Modeling damage and deformation in impact simulations. *Meteoritics & Planetary Science* 39:217–231.

Collins G. S., Davison T. M., Elbeshausen D., Robbins S. J., and Hynek B. M. 2011. The size-frequency distribution of elliptical impact craters. *Earth and Planetary Science Letters*, doi:10.1016/j.epsl.2011.07.023. forthcoming.

Elbeshausen D. and Wünnemann K. 2011. iSALE-3D: A three dimensional, multi-material, multi-rheology hydrocode and its applications to large-scale geodynamic processes. *Proceedings, 11th Hypervelocity Impact Society Symposium*, in press.

Elbeshausen D., Wünnemann K., and Collins G. S. 2009. Scaling of oblique impacts in frictional targets: Implications for crater size and formation mechanisms. *Icarus* 204:716–731.

Gault D. E. and Wedekind J. A. 1978. Experimental studies of oblique impact (abstract). *Proceedings, 9th Lunar and Planetary Science Conference*. pp. 3843–3875.

Gault D. E., Quaide W. L., and Oberbeck V. R. 1965. Interpreting ranger photographs from impact cratering studies. In *The nature of the lunar surface*, edited by Hess W. N., Henzel D. H., and O'Keefe J. A. Baltimore, MD: The Johns Hopkins Press. 125 p.

Gilbert G. K. 1893. The moon's face. A study of the origin of its features. *Bulletin of the Philosophical Society of Washington* 12:241–292.

Gisler G. R., Weaver R. P., Mader C. L., and Gittings M. L. 2004. Two- and three-dimensional asteroid impact simulations. *Computing in Science and Engineering* 6:46–55.

Hayhurst C. J., Ranson H. J., Gardner D. J., and Birnbaum N. K. 1995. Modelling of microparticle hypervelocity oblique impacts on thick targets. *International Journal of Impact Engineering* 17:375–386.

Holsapple K. A. 1987. The scaling of impact phenomena. *International Journal of Impact Engineering* 5:343–355.

Holsapple K. A. 1993. The scaling of impact processes in planetary sciences. *Annual Review of Earth and Planetary Sciences* 21:333–373.

Holsapple K. A. and Schmidt R. M. 1982. On the scaling of crater dimensions—2. Impact processes. *Journal of Geophysical Research* 87:1849–1870.

Holsapple K. A. and Schmidt R. M. 1987. Point source solutions and coupling parameters in cratering mechanics. *Journal of Geophysical Research* 92:6350–6376.

Housen R. K. and Holsapple K. A. 2003. Impact cratering on porous asteroids. *Icarus* 163:102–119.

International Nickel Company. 1968. *Properties of some metals and alloys*, 3rd ed. New York: International Nickel Company. 63 p.

Ivanov B. A. 2005. Numerical modeling of the largest terrestrial meteorite craters. *Solar System Research* 39:381–409.

Ivanov B. A. and Artemieva N. A. 2002. Numerical modeling of the formation of large impact craters. *Catastrophic events and mass extinctions: Impacts and beyond*. Special Paper 356. pp. 619–630.

Ivanov B. A., Deniem D., and Neukum G. 1997. Implementation of dynamic strength models into 2D hydrocodes: Applications for atmospheric breakup and impact cratering. *International Journal of Impact Engineering* 20:411–430.

Kearsley A. T., Graham G. A., Burchell M. J., Cole M. J., Dai Z. R., Teslich N., Bradley J. P., Chater R., Wozniakiewicz P. A., Spratt J., and Jones G. 2007. Analytical scanning and transmission electron microscopy of laboratory impacts on Stardust aluminum foils: Interpreting impact crater morphology and the composition of impact residues. *Meteoritics & Planetary Science* 42:191–210.

Kearsley A. T., Graham G. A., Burchell M. J., Cole M. J., Wozniakiewicz P., Teslich N., Bringa E., Hörz F., Blum J., and Poppe T. 2008. Micro-craters in aluminum foils: Implications for dust particles from comet Wild 2 on NASA's Stardust spacecraft. *International Journal of Impact Engineering* 35:1616–1624.

Love S. G., Hörz F., and Brownlee D. E. 1993. Target porosity effects in impact cratering and collisional disruption. *Icarus* 105:216–224.

Marinova M. M., Aharonson O., and Asphaug E. 2011. Geophysical consequences of planetary-scale impacts into a Mars-like planet. *Icarus* 211:960–985.

Melosh H. J. 1989. *Impact cratering: A geologic process*. New York: Oxford University Press. 245–256.

Melosh H. J. and Ivanov B. A. 1999. Impact crater collapse. *Annual Review of Earth and Planetary Sciences* 27:385–415.

Melosh H. J., Ryan E. V., and Asphaug E. 1992. Dynamic fragmentation in impacts: Hydrocode simulation of laboratory impacts. *Journal of Geophysical Research* 97:14735–14759.

Ohnaka M. 1995. A shear failure strength law of rock in the brittle-plastic transition regime. *Geophysical Research Letters* 22:25–28.

Parker E. R. 1967. *Materials data book for engineers and scientists*. New York: McGraw-Hill. 398 p.

Pierazzo E. and Collins G. S. 2004. A brief introduction to hydrocode modeling of impact cratering. In *Cratering in marine environments and on ice*, edited by Dypvik H., Burchell M., and Claeys P. New York: Springer. pp. 323–340.

Pierazzo E. and Melosh H. J. 2000a. Hydrocode modeling of oblique impacts: The fate of the projectile. *Meteoritics & Planetary Science* 35:117–130.

Pierazzo E. and Melosh H. J. 2000b. Melt production in oblique impacts. *Icarus* 145:252–261.

Pierazzo E. and Melosh H. J. 2000c. Understanding oblique impacts from experiments, observations, and modeling. *Annual Review of Earth and Planetary Sciences* 28:141–167.

Pierazzo E., Artemieva N., Asphaug E., Baldwin E. C., Cazamias J., Coker R., Collins G. S., Crawford D. A., Davison T., Elbeshausen D., Holsapple K. A., Housen K. R., Korycansky D. G., and Wünnemann K. 2008. Validation of numerical codes for impact and explosion cratering: Impacts on strengthless and metal targets. *Meteoritics & Planetary Science* 43:1917–1938.

Schmidt R. M. and Housen K. R. 1987. Some recent advances in the scaling of impact and explosion cratering. *International Journal of Impact Engineering* 5:543–560.

Schultz P. H. and Lutz-Garihan A. B. 1982. Grazing impacts on Mars—A record of lost satellites. *Proceedings, 13th Lunar and Planetary Science Conference*. pp. A84–A96.

Shoemaker E. M. 1962. Interpretation of lunar craters. In *Physics and astronomy of the Moon*, edited by Kopal Z. New York and London: Academic Press. pp. 283–359.

Shuvalov V. V. 2003. Cratering process after oblique impacts. In *Large meteorite impacts. Proceedings, 3rd International Conference on Large Meteorite Impacts*, abstract #4130.

Shuvalov V. and Trubetskaya I. 2007. Numerical modeling of the formation of the Eltanin submarine impact structure. *Solar System Research* 41:56–64.

Shuvalov V. and Trubetskaya I. 2008. Numerical simulation of the LCROSS impact experiment. *Solar System Research* 42:1–7.

Tillotson J. M. 1962. Metallic equation of state for hypervelocity impact. General Atomic Report GA-3216:141.

Wünnemann K., Collins G. S., and Melosh H. J. 2006. A strain-based porosity model for use in hydrocode simulations of impacts and implications for transient crater growth in porous targets. *Icarus* 180:514–527.

Wünnemann K., Collins G. S., and Osinski G. R. 2008. Numerical modelling of impact melt production in porous rocks. *Earth and Planetary Science Letters* 269:529–538.